THE JOURNAL OF PHYSICAL CHEMISTRY LETTERS
A JOURNAL OF THE AMERICAN CHEMICAL SOCIETY

pubs.acs.org/JPCL Letter

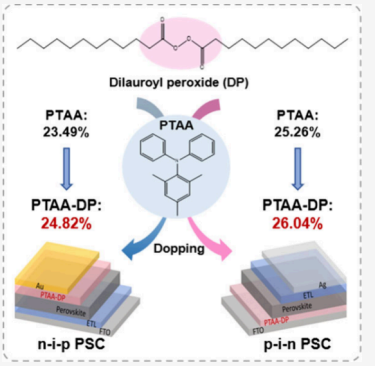
Hydrophobic Dilauroyl Peroxide Improves the Electrical Performance and Stability of PTAA in both n-i-p and p-i-n Perovskite Solar Cells

Zhineng Lan, Meng Wan, Huilin Yan, Hao Huang,* Benyu Liu, Yi Lu, Yingying Yang, Yi Suo, Guanzheng Zhang, Shuxian Du, Qiang Zhang, Zhiwei Wang, Tongtong Jiang, Changxu Sun, Shujie Qu, Luyao Yan, Peng Cui, and Meicheng Li*

Cite This: https://doi.org/10.1021/acs.jpclett.6c02136 Read Online

ACCESS | Metrics & More | Article Recommendations | Supporting Information

ABSTRACT: Stability degradation plagues both regular n-i-p and inverted p-i-n perovskite solar cells (PSCs), with the organic hole transport layer (HTL) constituting a key restricting factor. Poly(triarylamine) (PTAA) possesses intrinsic polymer characteristics and excellent thermal stability, rendering it a competitive candidate for high-performance PSCs applicable to both device structures. However, challenging p-doping procedures and vulnerability to humidity restrict its utilization. Herein, we introduced a hydrophobic dilauroyl peroxide (DP) with oxidation ability and a long-chain alkanes structure into the PTAA. Upon cleavage of the peroxide bond (−O−O−) of DP, two decanoyl free radicals are generated. These radicals seize the lone pair of electrons on the N atom of the triarylamine in PTAA, oxidizing PTAA into a positively charged radical $PTAA^{\bullet+}$, thereby achieving p-type doping of PTAA. This doping process enhances the electrical properties and transport characteristics of PTAA. Besides, the introduction of long-chain alkyl groups enhances the hydrophobicity of the PTAA film, increasing the water contact angle from 60.18° to 80.39°. As a result, the champion PCE of n-i-p PSCs increased from 23.49% to 24.82%, while that of p-i-n PSCs increased from 25.26% to 26.04%. Moreover, the humidity stability and thermal stability of the PSCs are enhanced. As a result, after the PSC aged for approximately 4752 h at 25 °C and 45% relative humidity, it still maintained 97% of its initial PCE.



In recent years, perovskite solar cells (PSCs) have achieved rapid development due to their excellent photoelectric performance, low preparation cost, and simple process flow. Currently, the regular n-i-p and inverted p-i-n structures represent the two mainstream technical routes for PSCs.[1,2] The power conversion efficiency (PCE) of PSCs based on both structures has exceeded 26% and continues to break records.[3] Meanwhile, in response to the demands of large-scale and industrialized applications, the large-scale preparation process of PSCs has also developed rapidly, laying a solid technological foundation for their commercial application.[4,5] However, compared with the rapidly advancing PCE and gradually maturing preparation processes, the insufficient stability of PSCs remains the core bottleneck restricting their industrialization and practical application.[6−9] Among the numerous factors affecting PSCs' stability, the degradation induced by hole transport layer (HTL) materials stands out as a key issue. This problem is widespread in both n-i-p and p-i-n structures of PSCs, serving as a common obstacle that limits further stability improvements in both types of PSCs.[10−12] Therefore, there is an urgent need to develop stable HTL materials and explore optimization strategies to enhance PSCs' PCE and long-term stability simultaneously.

Currently, researchers have conducted extensive studies from the perspective of the HTL to address the stability issues of PSCs with different structures, achieving positive progress. In n-i-p PSCs, research has largely focused on the modification and optimization of the Spiro-OMeTAD HTL, employing doping strategies such as metal−organic salts, ionic liquids, and electrochemical methods to enhance its performance and stability.[13−16] Meanwhile, through chemical modification of the Spiro-OMeTAD backbone (e.g., introducing alkoxy groups, fluorinated moieties, or conjugated extension units), a series of novel spiro-type hole transport materials has been synthesized,[17,18] exhibiting higher stability. In p-i-n PSCs, research efforts are concentrated on several directions: First, to address the interfacial recombination and stability issues of the inorganic HTL of nickel oxide (NiOx) by introducing strategies such as valence state regulation and interfacial

Received: June 28, 2026
Revised: August 3, 2026
Accepted: August 4, 2026

ACS Publications © XXXX American Chemical Society

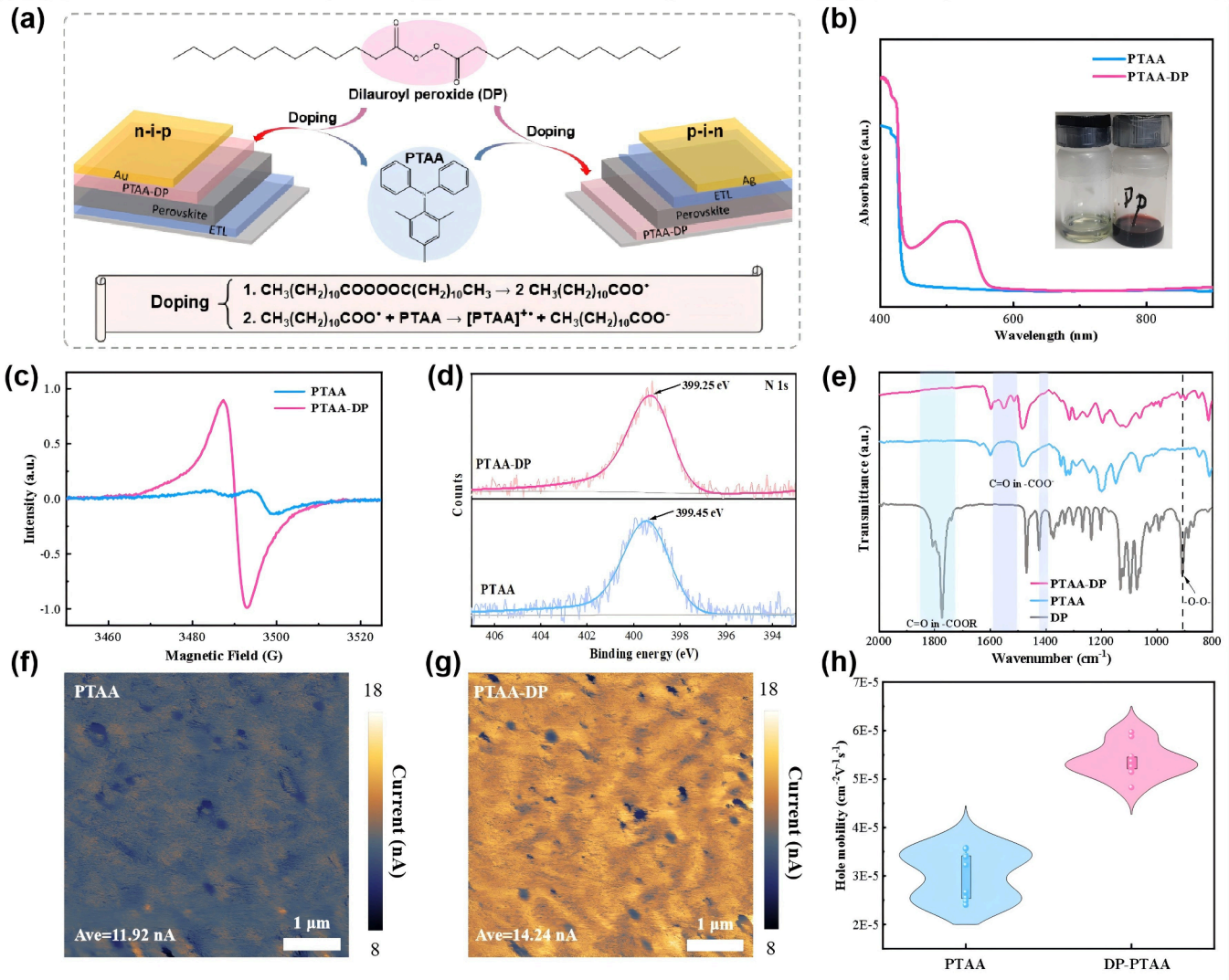


Figure 1. DP oxidation doping strategy and its influence on PTAA film. (a) Mechanism diagram of DP oxidation doping of PTAA and its application in n-i-p and p-i-n PSCs. (b) The absorption spectra of PTAA and PTAA-DP solutions. (c) The EPR spectra of PTAA and PTAA-DP solutions. (d) XPS spectra of N *1s* peaks of PTAA film and PTAA-DP film. (e) FTIR spectra of DP, PTAA, and PTAA-DP film. (f,g) C-AFM images of PTAA film and PTAA-DP film. (h) Statistical graph of hole mobility of PTAA and PTAA-DP devices.

passivation layers.[19,20] Second, strategies such as anchoring group design and multicomponent blending are adopted to address the issues of easy detachment and degradation of the self-assembled monolayer (SAM), thereby enhancing the adhesion and chemical stability of SAM.[21−24] In addition, the development of new conjugated polymer hole transport materials, through strategies such as constructing donor−acceptor conjugated main chains and introducing functional side chains, has significantly enhanced the hole mobility and interfacial compatibility of polymer materials, providing a new material option for the stability optimization of PSCs.[25−27]

Among various hole transport materials, conjugated polymer materials have gradually become the research focus of high-stability PSCs due to their excellent intrinsic stability.[28,29] Among them, polyterphenylamine (PTAA) stands out due to its unique molecular structure and comprehensive performance. The main chain of PTAA is composed of triarylamine units alternately connected, featuring excellent conjugation and structural rigidity, which endows it with outstanding hole transport capacity and high thermal stability.[30] More importantly, compared with Spiro-OMeTAD, commonly used in n-i-p structure and SAM and NiOx in p-i-n structure, PTAA can not only withstand the high temperature and high-energy particle bombardment during the evaporation process of the metal electrode in the n-i-p structure, but also endure the high-temperature annealing process required for the preparation of perovskite layers in the p-i-n structure. This unique advantage makes it one of the few hole transport materials that can simultaneously and perfectly accommodate the two mainstream structures of PSCs.[31,32]

Although PTAA has significant comprehensive performance advantages, there are still two core shortcomings at the present stage. On the one hand, the doping process of PTAA is quite challenging, making it difficult to achieve full doping and resulting in insufficient doping stability.[33,34] To address this issue, various strategies including p-type molecular dopants[35] and Lewis acid oxidative dopants[34] have been developed to boost the hole conductivity of PTAA films, yet most existing systems still face an inherent trade-off among doping efficiency, long-term doping durability, and process compatibility, which can eventually cause doping failure and impair the PCE and long-term stability of PSCs. On the other hand, the commonly

https://doi.org/10.1021/acs.jpclett.6c02136
J. Phys. Chem. Lett. XXXX, XXX, XXX−XXX

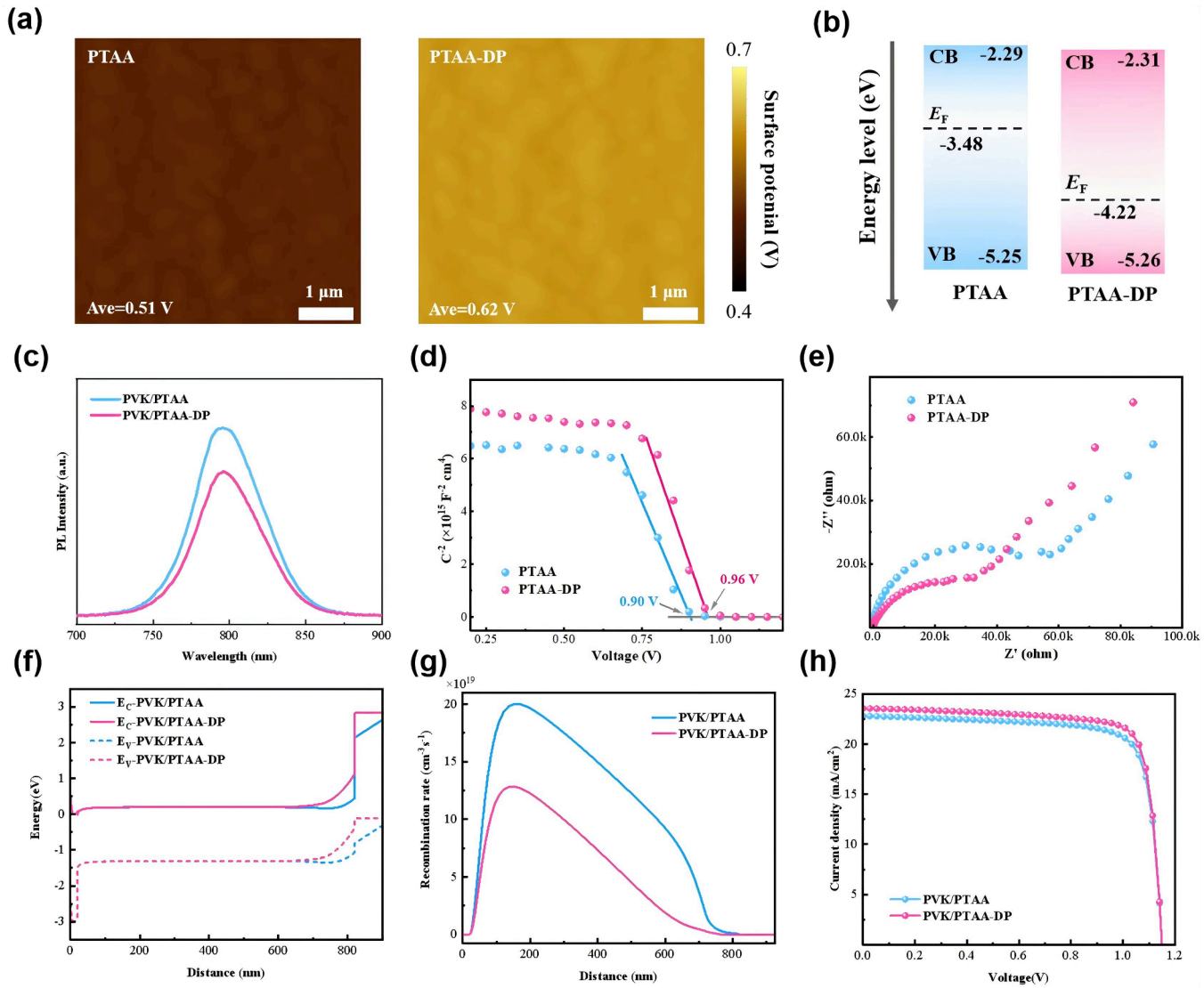


Figure 2. Effects of DP oxidation doping on the electrical properties of PTAA. (a) KPFM images of PVK/PTAA film and PVK/PTAA-DP film. (b) Energy level structure diagram of the PTAA film before and after DP oxidation doping. (c) PL spectra of glass/perovskite/PTAA (PTAA-DP) films. (d) Mott−Schottky curves of n-i-p PSCs with PTAA and PTAA-DP. (e) EIS curves of n-i-p PSCs with PTAA and PTAA-DP. (f) The simulated energy band structure of PSCs before and after DP oxidation doping. (g) The simulated carrier recombination distribution of PSCs. (h) The simulated *J*−*V* curves of PSCs.

used combination of lithium salts and tBP is sensitive to environmental humidity and prone to absorbing moisture, which leads to the formation of holes in the HTL, resulting in problems such as material degradation and ion migration, seriously restricting the humidity stability of the PSCs.[15,36,37] Though emerging nonionic fluorinated dopants[38] and inorganic dopant[39] have mitigated the hygroscopic problem to some extent, they still struggle to simultaneously achieve high doping efficiency, excellent environmental stability, and facile solution processability. Therefore, it is necessary to carry out targeted research on PTAA regulation, improve its doping performance and stability, and explore its influence on the performance of perovskite solar cells with different structures.

Hence, we introduced dilauroyl peroxide (DP) into the traditional PTAA HTL. By leveraging the strong oxidation capacity of the peroxide bond (−O−O−) in the DP molecule, we achieved sufficient and controllable oxidation of PTAA, significantly improving its electrical properties and transport characteristics. This has achieved simultaneous improvements in the PCEs of n-i-p and p-i-n PSCs. The champion PCE of n-i-p PSCs increased from 23.49% to 24.82%, while that of p-i-n PSCs increased from 25.26% to 26.04%. At the same time, based on the hydrophobic property of the long-chain alkyl group of the DP molecule, the moisture absorption problem of lithium salts is effectively alleviated, and the humidity stability and thermal stability of the PSCs are enhanced. As a result, after the PSC aged for approximately 4752 h at 25 °C and 45% relative humidity, it still maintained 97% of its initial PCE. After being aged at 85 °C for 1080 h, it still maintained 85% of its initial PCE.

PTAA features outstanding hole transport capability, intrinsic thermal stability, and a compatible energy level structure, and can be simultaneously applied to both n-i-p and p-i-n structures of PSCs (Figure 1a), demonstrating unique structural universality. However, in practical applications, PTAA still faces pain points such as the difficulty of p-type doping and poor humidity stability caused by the moisture absorption of dopants. To this end, we have designed and

https://doi.org/10.1021/acs.jpclett.6c02136
J. Phys. Chem. Lett. XXXX, XXX, XXX−XXX

adopted dopants that simultaneously possess strong oxidation capacity and hydrophobic properties, such as dilauroyl peroxide (DP), to address the doping and stability issues faced by PTAA. DP features a highly symmetrical molecular structure with a peroxide bond (−O−O−) as the core, flanked by two lauroyl groups on both sides (Figure 1a). Among them, the peroxide bond has low bond energy and tends to cleave easily, which endows DP with strong oxidative activity. Meanwhile, the long alkyl chains with high hydrophobicity can effectively reduce the moisture adsorption of the PTAA HTL.

First, we introduce DP into the PTAA solution. It can be clearly observed that after adding DP, the solution color significantly changed from light yellow to deep red, which directly reflects the oxidation doping phenomenon of DP on PTAA (Figure 1b). Even when using powder for mixing, a similar color change occurred (Figure S1). Further, through the ultraviolet absorption spectrum, it can be observed that in the range of 500−550 nm, there are clearly new generated absorption peaks related to $PTAA^{+\bullet}$ (Figure 1b). Similarly, from the electron paramagnetic resonance (EPR) spectrum, it can also be observed that a large number of free radicals were generated in the PTAA film after DP oxidation (Figure 1c).

To further determine the oxidation doping mechanism of DP on PTAA, first, XPS was used to analyze the chemical environment of the N atoms in PTAA. The results showed that after introducing DP, the N *1s* peak of PTAA shifted from 399.45 to 399.25 eV, indicating that DP achieved the oxidation doping of PTAA by seizing the lone pair of electrons on the N atoms, resulting in $PTAA^{\cdot+}$ (Figure 1d). On this basis, Fourier transform infrared (FTIR) spectroscopy was used to further track the evolution of functional groups of DP molecules during the doping process (Figure 1e). In the FTIR spectrum of pristine DP, a characteristic stretching vibration peak of the peroxide bond is observed at approximately 900 cm^{-1}, along with a C═O stretching vibration peak of the −COOR group at around 1800 cm^{-1}. After blending PTAA with DP, both of the above characteristic peaks disappear completely, while a new C═O stretching vibration peak assigned to the $-COO^-$ group emerges at approximately 1500 cm^{-1}. Based on the above characterization results, the complete doping mechanism can be deduced: the −O−O− at the center of the DP molecule undergoes homolytic cleavage to generate two decanoyl free radicals; these radicals abstract the lone-pair electrons from the nitrogen atoms of the triarylamine units in PTAA and oxidize neutral PTAA into $PTAA^{\cdot+}$ radical cations, thus accomplishing the oxidative doping process (Figure 1a and Figure S2).

After confirming the effective oxidation doping of DP on PTAA, we conducted Conductive AFM (C-AFM) tests on the films before and after doping. The results show that the average surface current of the PTAA film is 11.92 nA, while the overall average current of the PTAA-DP film has increased to 14.24 nA, which is consistent with the test results of the films' conductivity (Figures 1f and 1g and Figure S3). Moreover, the hole mobility of the 9 samples after oxidation doping by DP also increased from an average of 3.03×10^{-5} to 5.39×10^{-5} $cm^{-2}V^{-1}s^{-1}$ (Figure 1h), indicating that the large number of PTAA free radical cations generated after oxidation doping enhanced the conductivity and hole migration ability of the material, providing a good foundation for the overall PCE improvement of the PSCs.

In the overall structure of PSCs, the performance of HTL not only depends on its electrical conductivity and mobility, but also its energy level structure is equally crucial. Interface energy level matching is the key to regulating the carrier behavior at the interface with perovskite layers, which determines the separation efficiency and transport rate of interface carriers. We first used Kelvin probe force microscopy (KPFM) to test the surface potential of PTAA films before and after oxidation doping. The results show that the average surface potential of the PTAA-DP film is significantly higher than that of the PTAA film, indicating that the Fermi level (E_F) has moved closer to the valence band top (Figure 2a). Furthermore, we conducted tests and analyses on the two films by combining ultraviolet photoelectron spectroscopy (UPS) and UV absorption spectroscopy to determine the energy level structure of the films (Figure 2b, Figures S4 and S5). The oxidation doping effect of DP causes the Fermi level of the original PTAA film to shift downward, and the conductive type of the film becomes more p-type, which is consistent with the KPFM results.

We further employed photoluminescence spectroscopy (PL), Mott−Schottky (MS), and electrochemical impedance spectroscopy (EIS) to conduct comprehensive tests, thereby verifying the optimization effect of DP oxidation doping on the charge transfer efficiency at the PTAA/perovskite interface. First, in contrast, the photoluminescence spectra of samples spin-coated with PTAA-DP on the surface of the perovskite film exhibited a more significant quenching compared to those of samples spin-coated with PTAA, indicating that the DP-doped oxidized PTAA HTL can more efficiently extract the photogenerated holes from the perovskite active layer (Figure 2c). Further analysis of the fitting results of the TRPL data indicates that, compared with the PTAA sample, the rapid decay lifetime of the PTAA-DP sample has significantly decreased from 63.76 to 30.98 ns (Figure S6). At the same time, the average carrier lifetime after DP doping has decreased from 1838 to 1176 ns, which suggests that DP doping effectively accelerates the extraction of carriers at the PTAA/perovskite interface and optimizes the transport behavior of interface carriers. Meanwhile, the Mott−Schottky curve test results indicate that the built-in electric field (V_{bi}) of the PTAA-DP device is 0.96 V, which is higher than that of the PTAA device (0.90 V) (Figure 2d). A larger V_{bi} is more conducive to the separation driving force of photogenerated electron−hole pairs and transport of charge carriers. The EIS test results (Figure 2e) further confirm this conclusion. Compared with the PTAA device, the charge transfer impedance (Rct) of the PTAA-DP device has significantly decreased, which indicates that the resistance of charge transmission at the interface has been effectively reduced.

Based on the energy level structure obtained from the experiments, we further utilized the "Solar Cell capacitor Simulator-One Dimension" software to explore the impact of DP oxidation doping on carrier transport and PSCs' performance from a simulation perspective. The results show that after DP doping, the doping concentration increases, reducing the energy level offset and optimizing the interface energy level matching (Figure 2f). The carrier recombination distribution indicates that after DP oxidation doping, the carrier recombination at the PTAA and perovskite interfaces has been effectively suppressed (Figure 2g). Finally, we simulated and calculated the *J*−*V* curves of PTAA and PTAA-DP-based PSCs. It can be seen that due to the optimization of the energy level structure and the suppression of carrier recombination,

https://doi.org/10.1021/acs.jpclett.6c02136
J. Phys. Chem. Lett. XXXX, XXX, XXX−XXX

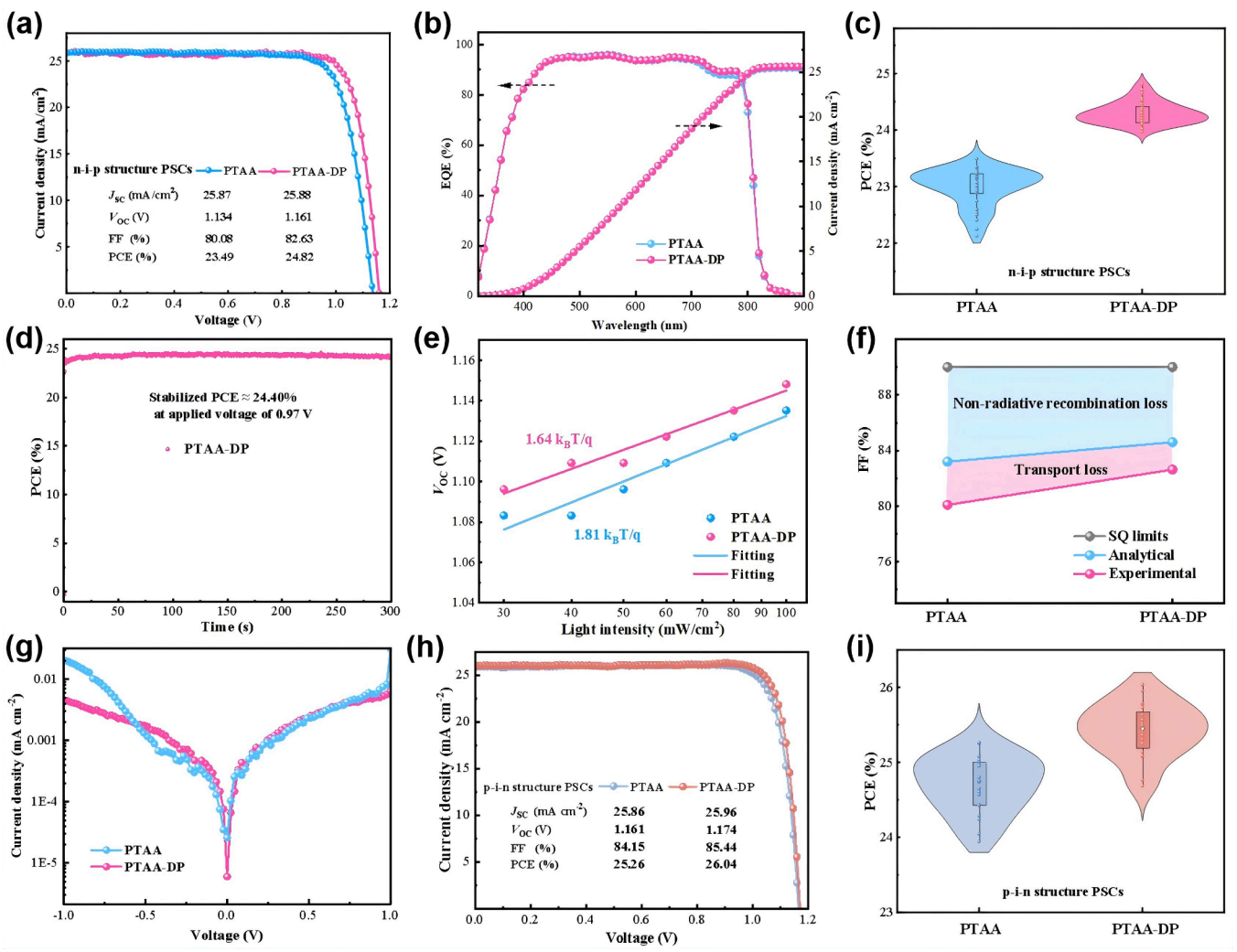


Figure 3. Photovoltaic performance of n-i-p and p-i-n PSCs with PTAA and PTAA-DP. (a) Reverse $J-V$ curves of champion n-i-p PSCs with PTAA and PTAA-DP. (b) EQE curves of n-i-p PSCs with PTAA and PTAA-DP. (c) Statistical results of PCEs of n-i-p PSCs with PTAA and PTAA-DP. (d) Monitoring of PTAA-DP-based n-i-p PSCs steady-state output efficiency. (e) Light-intensity dependence of V_{OC} of n-i-p PSCs with PTAA and PTAA-DP. (f) V_{OC} loss diagram of n-i-p PSCs with PTAA and PTAA-DP. (g) Dark $J-V$ curves of n-i-p PSCs with PTAA and PTAA-DP. (h) Reverse $J-V$ curves of champion p-i-n PSCs with PTAA and PTAA-DP. (i) Statistical results of PCEs of p-i-n PSCs with PTAA and PTAA-DP.

the PCE of the PSC has been improved accordingly after DP doping (Figure 2h).

The synergistic improvement of the characteristics of the HTL itself and the interface transport through DP oxidation doping provides an important foundation for the subsequent improvement of the PCE of the two structures of PSCs. Therefore, in order to assess the impact of DP oxidation doping on performance, we first constructed n-i-p PSCs (FTO/TiO_2/PVK/PTAA or PTAA-DP/Au) for testing. As shown in Figure 3a, the n-i-p PSCs with PTAA-DP obtain a champion PCE of 24.82% (short-circuit current density [J_{SC}] = 25.88 mA/cm^2, V_{OC} = 1.161 V, and fill factor [FF] = 82.63%), which was significantly higher than the champion PCE of 23.49% for the PTAA-based PSC, especially in terms of V_{OC} (1.131 V) and FF (80.08%) (Figure S7). The obtained integrated current values from external quantum efficiency (EQE) are 25.48 mA/cm^2 (PTAA) and 25.63 mA/cm^2 (PTAA-DP), respectively, which are not significantly different from the current values obtained from the $J-V$ test (Figure 3b). We conducted a statistical analysis of the photovoltaic parameters of each group of 35 PSCs, as shown in Figure 3c. The average PCE of the PTAA-DP-based PSCs was 24.30%, significantly higher than that of the PTAA-based PSCs (22.99%), and exhibited a more concentrated distribution. Similar results were observed for V_{OC}, FF, and J_{SC} (Figure S8). We also conducted steady-state power output measurements on the PTAA-DP-based PSCs. The results showed that after 300 s, the stable output efficiency of the PTAA-DP-based PSC was 24.40%, indicating good output stability (Figure 3d).

We further carried out variable light intensity tests and dark current tests to deeply explore the influence of DP oxidation doping on the carrier transport and recombination mechanism of the PSCs. The results of the variable light intensity test show that the ideal factor of the PTAA PSC is 1.81 K_BT/q, while that of the PTAA-DP-based PSC drops to 1.64 K_BT/q (Figure 3e). Meanwhile, the actual measured FF of the PTAA-DP-based PSC is significantly higher than that of the PTAA PSC, and the difference from the maximum FF calculated without considering charge transport loss is significantly smaller (Figure 3f). The dark current of the PTAA-DP PSCs was

https://doi.org/10.1021/acs.jpclett.6c02136
J. Phys. Chem. Lett. XXXX, XXX, XXX−XXX

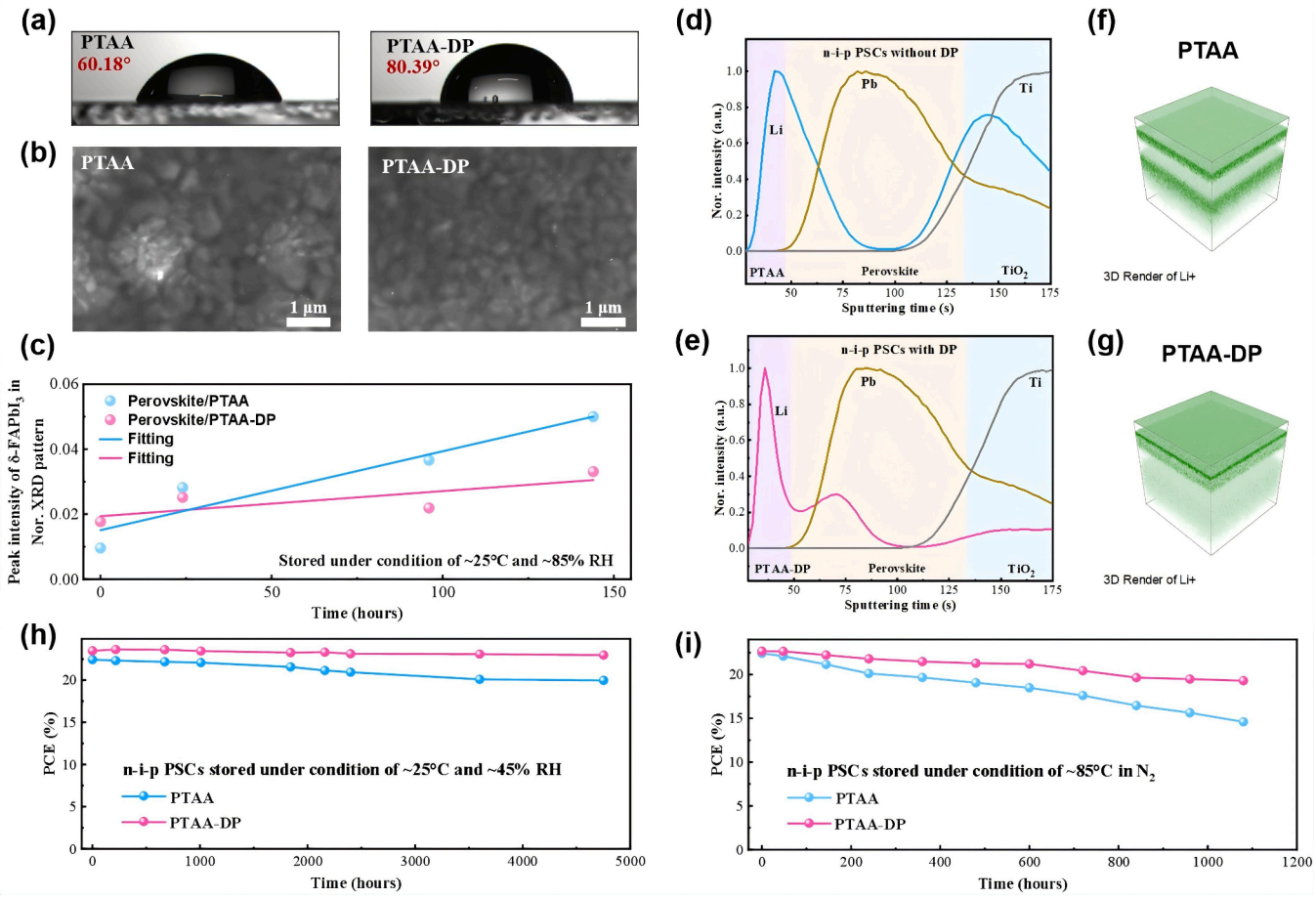


Figure 4. Humidity and heat stability of PSCs with PTAA and PTAA-DP. (a) The water contact angle test results of PTAA and PTAA-DP films. (b) SEM images of PTAA and PTAA-DP films after air exposure and aging. (c) The changes in the intensity of the nonphotoactive δ-$FAPbI_3$ in the perovskite/PTAA and perovskite/PTAA-DP films. (d) The TOF-SIMS spectra of n-i-p PSC with PTAA. (e) The TOF-SIMS spectra of n-i-p PSC with PTAA-DP. (f,g) The corresponding 3D rendering of the Li^+ distribution of n-i-p PSCs with PTAA-DP and PTAA-DP. (h) The humidity stability of unencapsulated n-i-p PSCs with PTAA and PTAA-DP. (i) The thermal stability of unencapsulated n-i-p PSCs with PTAA and PTAA-DP.

significantly reduced, which also indicates that the internal leakage current and the nonradiative recombination process were effectively suppressed in the PSCs (Figure 3g). The test results of variable light intensity and dark current are cross-verified with the characterization results of electrical performance, energy level structure, and interface characteristics in the previous text, indicating that DP oxidation doping optimizes the performance of the PTAA HTL from multiple aspects, providing strong support for the improvement of PSCs' PCE and stability.

After completing the mechanism analysis of the improvement of PTAA transport characteristics and the enhancement of PSCs performance by DP oxidation doping, we further applied the PTAA-DP HTL to the p-i-n PSCs to verify its structural universality. The transmission spectra of the films indicates that both the PTAA and PTAA-DP films have high transmittance within the range of 450−800 nm (Figure S9). Figure 3h shows the $J-V$ curve of the champion device of the p-i-n structure PSCs (FTO/PTAA or PTAA-DP/SAM/PVK/BCP/C60/Ag). In comparison, the p-i-n PSCs with PTAA-DP obtain a champion PCE of 26.04% (V_{OC} = 1.174 V, J_{SC} = 25.96 mA/cm^2, and FF = 85.44%), which was significantly higher than the champion PCE of 25.26% for the PTAA-based p-i-n PSC, especially in terms of V_{OC} (1.161 V) and FF (84.15%) (Figure S10). The corresponding EQE spectrum is shown in Figure S11. The statistical results of 20 PSCs in each group show that the average PCE of the PTAA-based PSCs is 24.70%, significantly lower than the average PCE of PTAA-DP PSCs (25.43%) (Figure 3i). Moreover, after DP oxidation doping, the average V_{OC} and FF were significantly improved, with the V_{OC} increasing from an average of 1.159 to 1.167 V and the FF increasing from an average of 83.35% to 85.01% (Figure S12). By effectively oxidizing the PTAA HTL through DP molecular doping and improving the energy levels and interface carrier transport, the PTAA HTL has been effectively promoted to be widely applicable in n-i-p and p-i-n structure PSCs and to enhance the PCE of both structure PSCs.

The DP molecule not only possesses the peroxide bonds that can effectively oxidize and regulate HTL, but also has two long-chain hydrophobic alkanes. This will help prevent the intrusion of external moisture and enhance the stability of the PSCs, especially in terms of humidity and heat stability. Figure 4a shows the water contact Angle test results of PTAA and PTAA-DP films, respectively, spin-coated on the perovskite surface. It can be clearly seen that after the addition of DP, the water contact Angle of the films has increased from 60.18° to 80.39°. In addition, a large number of white particles appeared on the surface of the PTAA film after air exposure and aging

https://doi.org/10.1021/acs.jpclett.6c02136
J. Phys. Chem. Lett. XXXX, XXX, XXX−XXX

(Figure 4b). This might be related to the agglomeration and porosity caused by the moisture absorption of lithium salts in the film. Furthermore, the aging test on the conductivity of the films also validate the enhanced air stability after incorporating of DP (Figure S13). As for the stability of perovskite film, we utilized XRD to monitor the changes in the intensity of the nonphotoactive δ phase perovskite in the perovskite/PTAA and perovskite/PTAA-DP films under high humidity aging conditions, and fitted the trend of these changes (Figure 4c). In contrast, the fitting slope of the perovskite/PTAA-DP film was significantly reduced, indicating that the water-induced phase transformation process of the PTAA-DP-coated perovskite film was slower. This confirmed that DP can effectively prevent water vapor penetration by enhancing hydrophobicity and effectively inhibiting the decomposition of the perovskite active layer.

Further, we adopted TOF-SIMS to explore the situation of Li^+ inside the PSCs. It can be seen that Li^+ in the PTAA-based PSCs has significantly migrated to the bottom interface of the perovskite film and accumulated at the interface (Figure 4d). In contrast, the degree of Li^+ migration in PTAA-DP-based PSCs is relatively low, and it is still mainly distributed in the HTL and the upper surface of perovskite, with a significantly lower content at the bottom interface of perovskite (Figure 4e). The 3D rendering of the Li^+ distribution can more clearly show this distribution difference (Figures 4f and 4g). Finally, we conducted humidity stability and thermal stability tests, taking the n-i-p structure PSCs as an example. As shown in Figure 4h, after approximately 4752 h of aging at 25 °C and 45%RH, the PTAA-DP-based PSC still maintained 97% of its initial PCE, while the PTAA-based PSC ultimately only maintained 89% of its initial PCE. Meanwhile, Figure 4i shows the performance changes of the PSCs when it is placed and aged in a dry nitrogen environment at 85 °C. Among them, the PCE of the PTAA-based PSCs has declined to 65% of the initial PCE after 1080 h of aging, while the PTAA-DP-based PSCs still maintain 85% of the initial PCE.

In summary, by introducing DP into the PTAA HTL, we modulate its electrical properties via oxidative doping and enhance its stability through increased hydrophobicity, which synergistic effect ultimately delivers simultaneous improvements in both the photovoltaic performance and stability of PSCs. As a result, the PCE of n-i-p PSCs increased from 23.49% to 24.82%, while that of p-i-n PSCs increased from 25.26% to 26.04%. Besides, after the n-i-p PSC was aged for approximately 4752 h at 25 °C and 45% relative humidity, it still maintained 97% of its initial PCE. After being aged at 85 °C for 1080 h, it still maintained 85% of its initial PCE. Our work provides a feasible technical approach to simultaneously address the doping performance and long-term stability issues of PTAA HTL, and offers an important technical reference for the universal application of PTAA HTL in PSCs with various device structures.

EXPERIMENTAL METHODS

Materals

FTO glass (~15 Ω) was purchased from Youxuan New Energy Technology Co. Ltd.; $TiCl_4$ (99.9%) was purchased from Aladdin; lead iodide (PbI_2, 99.999%), *N*,*N*-dimethylformamide (DMF, 99.9%), dimethyl sulfoxide (DMSO, 99.9%), and chlorobenzene (CB, 99.9%) were purchased from Sigma-Aldrich; formamidinium iodide (FAI, 99.8%), methylamine iodide (MAI, 99.9%), cesium iodide (CsI, 99.98%), 4-methoxyphenylethylamine hydroiodide (Meo-PEAI, 99.8%), methylammonium chloride (MACl, 99.99%), *tert*-butylpyridine (tBP) and lithium bis (trifluoromethylsulfonyl) imide (LiTFSI, 99%) were purchased from Xi'an Polymer Light Technology Corp; dilauroyl peroxide (DP), poly[bis(4-phenyl)(2,4,6-trimethylphenyl)amine] (PTAA, 99.8%), methoxy-phenethylammonium iodide (MeO-PEAI), isopropanol (IPA, 99.99%) and acetonitrile (ACN, 99.99%) were purchased from Beijing InnoChem Science & Technology Co., Ltd. All chemicals were employed as received without further modifications after purchase.

Device Fabrication

Preparation of n-i-p structure PSCs: FTO glass substrate preparation: The FTO glass substrate was cleaned with deionized water, ethanol, and deionized water using ultrasonic cleaning for 15 min each. After drying with high-purity N_2, the substrate was processed under ultraviolet ozone (UVO) for 15 min to achieve a hydrophilic surface. TiO_2 ETL preparation: A mixture of $TiCl_4$ (4 mL) and deionized water (200 mL) was stirred to obtain a TiO_2 precursor. The FTO substrate was then immersed in the precursor and placed in a water bath at 70 °C for 40 min to form a compact TiO_2 electron transport layer. Preparation of perovskite: The 1.54 M $FA_{0.85}MA_{0.1}Cs_{0.05}PbI_3$ (DMF: DMSO, 4:1 volume/volume) precursor was spin-coated on FTO/TiO_2 substrate at 3800 rpm for 20 s, 970 μL diethyl ether as antisolvent was dripped at 14 s before the end of spin-coating. Then, the film was transferred to air for annealing at 110 °C for 10 min. The Meo-PEAI solution was prepared by mixing 4.5 mg Meo-PEAI in 1 mL of isopropanol. The Meo-PEAI layer was spin-coated at 4000 rpm for 30 s above the perovskite. Preparation of HTLs: The PTAA solution was prepared by mixing 30 mg PTAA in 1 mL chlorobenzene with 18 μL tBP, 8 μL Li-TFSI salt (520 mg/mL in ACN). The PTAA-DP solution was prepared by adding 0.7 mg/mL of dilauroyl peroxide to the PTAA solution. The PTAA and PTAA-DP HTLs were spin-coated at 4000 rpm for 30 s above the perovskite layer, then transferred to a hot plate for annealing at 100 °C for 5 min. Preparation of electrode: An Au electrode (60 nm) was deposited by thermal evaporation to obtain PSCs. Preparation of p-i−n structure PSCs: Hole transport layer (HTL) preparation: The PTAA or PTAA−DP solution used in a regular structured device was diluted to 0.5 mg/mL and spin-coated on a cleaned FTO substrate at 4000 rpm for 30 seconds, followed by annealing at 100° C for 5 minutes. Then, the MeO−PACz solution (0.4 mg/mL in IPA) was spin-coated on PTAA at 3000 rpm for 30 seconds, followed by annealing at 100°C for 10 minutes. Perovskite film preparation: 1.5 M perovskite solution ($FA_{0.85}MA_{0.1}Cs_{0.05}PbI_3$ in a mixed solvent of DMF: DMSO with volume/volume of 4:1) was spin-coated on HTL at 1000 rpm for 10 seconds and 5000 rpm for 30 seconds, 200 μL CB was dripped onto the center of the film at 5 seconds before the end of spin-coating. The deposited perovskite film was then annealed at 100°C for 30 minutes. Then, PEACl solution (1 mg/mL in IPA) was spin−coated on the perovskite film at 4000 rpm for 30 seconds, followed by annealing at 100°C for 3 minutes. Electron transport layer (ETL) preparation: C60 and BCP were deposited on top of passivated perovskite by thermal evaporation with thicknesses of 15 nm and 7 nm, respectively. Ag electrode preparation: An Ag electrode (100 nm) was deposited by thermal evaporation on top of ETL.

https://doi.org/10.1021/acs.jpclett.6c02136
J. Phys. Chem. Lett. XXXX, XXX, XXX−XXX

Characterization

The device efficiency was measured using a Keithley 2400 source meter with a scan rate of 13 mV s^{-1} under simulated AM 1.5G illumination (100 mW cm^{-2}) provided by a 150 W Class AAA solar simulator (XES-40S1, SAN-EI). The light intensity of the solar simulator was calibrated using a National Institute of Metrology certified silicon solar. The external quantum efficiency and integrating current of perovskite solar cells were measured using QE-R systems (Enli Tech) under AC pattern conditions. Cold field-emission scanning electron microscopy (SEM) using a HITACHI SU8010 instrument was used to analyze the surface morphology of the samples. Fourier transform infrared spectroscopy (FTIR) using a Bruker instrument with a scanned region from 4000 to 600 cm^{-1} wavenumber. Ultraviolet photoelectron spectroscopy (UPS) was performed using an ESCALAB 250Xi system to analyze the surface composition and electronic structure of the samples. Ultraviolet−visible (UV−vis) spectra were recorded using a SHIMADZU UV-2600 spectrophotometer. Steady-state photoluminescence (PL) was employed to study the carrier behavior of the samples. The excitation wavelength used for these measurements was 470 nm. Atomic force microscopy (AFM) using an FMNanoview 1000 instrument was used to characterize the surface morphology of the samples. Kelvin probe force microscopy (KPFM) and conducting atomic force microscopy (C-AFM) were utilized to measure the surface potential and contact current of the films. The electron paramagnetic resonance (EPR) was performed on Bruker EMX PLUS instrument. To characterize the existence and its migration, Time-of-flight secondary ion mass spectrometry (TOF-SIMS 5-100, IONTOF GmbH) was performed.

SCAPS-1D Introduction

Solar Cell Capacitance Simulator-one Dimension (SCAPS-1D) version 3.3.11 was used in this work to build a perovskite solar cell model, validating the effectiveness of the doping strategies employed. SCAPS-1D was developed by Marc Burgelman and his colleagues at the University of Ghent, Belgium.

■ ASSOCIATED CONTENT

Supporting Information

The Supporting Information is available free of charge at https://pubs.acs.org/doi/10.1021/acs.jpclett.6c02136.

Materials characterization, photographs, mechanism schematic diagram, device characterization, electrical conductivity, UPS, TRPL, transmittance spectra, device characterization, forward $J-V$ curves, photovoltaic performance statistical graph, EQE, stability, and conductivity stability (PDF)

■ AUTHOR INFORMATION

Corresponding Authors

Hao Huang − *State Key Laboratory of Alternate Electrical Power System with Renewable Energy Sources, School of New Energy, North China Electric Power University, Beijing 102206, China*; Email: hhuang@ncepu.edu.cn

Meicheng Li − *State Key Laboratory of Alternate Electrical Power System with Renewable Energy Sources, School of New Energy, North China Electric Power University, Beijing 102206, China*; Email: mcli@ncepu.edu.cn

Authors

Zhineng Lan − *State Key Laboratory of Alternate Electrical Power System with Renewable Energy Sources, School of New Energy, North China Electric Power University, Beijing 102206, China*

Meng Wan − *State Key Laboratory of Alternate Electrical Power System with Renewable Energy Sources, School of New Energy, North China Electric Power University, Beijing 102206, China*

Huilin Yan − *State Key Laboratory of Alternate Electrical Power System with Renewable Energy Sources, School of New Energy, North China Electric Power University, Beijing 102206, China*

Benyu Liu − *Beijing Huairou Laboratory, Beijing 101400, China*

Yi Lu − *State Key Laboratory of Alternate Electrical Power System with Renewable Energy Sources, School of New Energy, North China Electric Power University, Beijing 102206, China*

Yingying Yang − *State Key Laboratory of Alternate Electrical Power System with Renewable Energy Sources, School of New Energy, North China Electric Power University, Beijing 102206, China*

Yi Suo − *State Key Laboratory of Alternate Electrical Power System with Renewable Energy Sources, School of New Energy, North China Electric Power University, Beijing 102206, China*

Guanzheng Zhang − *State Key Laboratory of Alternate Electrical Power System with Renewable Energy Sources, School of New Energy, North China Electric Power University, Beijing 102206, China*

Shuxian Du − *State Key Laboratory of Alternate Electrical Power System with Renewable Energy Sources, School of New Energy, North China Electric Power University, Beijing 102206, China*

Qiang Zhang − *State Key Laboratory of Alternate Electrical Power System with Renewable Energy Sources, School of New Energy, North China Electric Power University, Beijing 102206, China*

Zhiwei Wang − *State Key Laboratory of Alternate Electrical Power System with Renewable Energy Sources, School of New Energy, North China Electric Power University, Beijing 102206, China*

Tongtong Jiang − *State Key Laboratory of Alternate Electrical Power System with Renewable Energy Sources, School of New Energy, North China Electric Power University, Beijing 102206, China*

Changxu Sun − *State Key Laboratory of Alternate Electrical Power System with Renewable Energy Sources, School of New Energy, North China Electric Power University, Beijing 102206, China*

Shujie Qu − *State Key Laboratory of Alternate Electrical Power System with Renewable Energy Sources, School of New Energy, North China Electric Power University, Beijing 102206, China*

Luyao Yan − *State Key Laboratory of Alternate Electrical Power System with Renewable Energy Sources, School of New Energy, North China Electric Power University, Beijing 102206, China*

Peng Cui − *State Key Laboratory of Alternate Electrical Power System with Renewable Energy Sources, School of New Energy, North China Electric Power University, Beijing 102206, China*

https://doi.org/10.1021/acs.jpclett.6c02136
J. Phys. Chem. Lett. XXXX, XXX, XXX−XXX

Complete contact information is available at:
https://pubs.acs.org/10.1021/acs.jpclett.6c02136

Author Contributions

M.L., Z.L., and H.H. conceived the idea. M.L., H.H., and P.C. guided the work as supervisors. Z.L. and M.W. did experimental designs, device fabrication, and data analysis. H.Y and Y.L. participated in the device fabrication and some characterizations. Q.Z. and B.L. contributed to the simulation and calculation. S.Q., Z.W., and Y.S. assisted with some characterization tests. Y.Y. and S.D. contributed to the ion migration characterization. Z.L. and H.H. wrote the first draft of the manuscript. T.J., L.Y., and C.S. assisted in revising and polishing the manuscript language. All authors discussed the results and contributed to the revisions of the manuscript.

Notes

The authors declare no competing financial interest.

■ ACKNOWLEDGMENTS

This work is supported partially by the National Natural Science Foundation of China (Grant nos. 52232008, 52402254, 52102245, and 22409061), Beijing Natural Science Foundation (26JL001, Z240024), the Key Research and Development Program sponsored by the Ministry of Science and Technology (MOST) (Grant nos. 2022YFB4200301), the project of China Three Gorges Corporation named key technologies of intelligent joint regulation and operation with grid connected friendly in power station group of wind, solar photovoltaic and energy storage (WWKY-2021-0173), the Fundamental Research Funds for the Central Universities (2023MS042, 2023MS047) and the NCEPU "Double First-Class" Program.

■ REFERENCES

(1) Zhang, L.; Zhang, M.; Wang, H.; Li, Z.; Zhang, Z.; Song, Y.; Song, X.; Wang, S.; Chen, J.; Li, W.; Dong, H.; Wang, F.; Liu, Y.; Li, X.; Yuan, J.; Ma, W.; Zhang, Y.; Liu, S.; Gao, F.; Wu, Z.; Yang, Z.; Hao, F.; Zhao, K.; Jin, Z.; Yan, K.; Chang, J.; Cao, J.; Wang, J.; Zhang, X.; Dong, Q.; Gao, P.; Zhao, Y.; Xiao, L.; Ding, Y.; Ding, L. Diverse perovskite solar cells: Progress, challenges, and perspectives. *Adv. Mater.* **2026**, *38*, No. e12221.

(2) Xu, C.; Hang, P.; Kan, C.; Guo, X.; Song, X.; Xu, C.; You, G.; Liao, W.-Q.; Zhu, H.; Wang, D.; Chen, Q.; Hong, Z.; Xiong, R.-G.; Yu, X.; Zuo, L.; Chen, H. Molecular ferroelectric self-assembled interlayer for efficient perovskite solar cells. *Nat. Commun.* **2025**, *16*, 835.

(3) Best research-cell efficiency chart: https://www.nrel.gov/pv/cell-efficiency.

(4) Yin, R.; Wu, Y.; Huang, Z.; Vasenko, A. S.; Xu, S.; Zhou, H. Fabricating perovskite films for solar modules from small to large scale. *Adv. Funct. Mater.* **2025**, *35*, No. 2419184.

(5) Harit, A. K.; He, Z.-F.; Kuang, Y.; Merckx, T.; Aguirre, A.; Li, M.; Xiao, K.; Wang, X.; Hou, Y.; Yan, B.; Tan, H.; Aernouts, T.; Krishna, A. Taking perovskite photovoltaics from promise to product. *Nature Reviews Clean Technology* **2026**, *2*, 453−466.

(6) Zhu, H.; Teale, S.; Lintangpradipto, M. N.; Mahesh, S.; Chen, B.; McGehee, M. D.; Sargent, E. H.; Bakr, O. M. Long-term operating stability in perovskite photovoltaics. *Nature Reviews Materials* **2023**, *8*, 569−586.

(7) Nazir, G.; Lee, S.-Y.; Lee, J.-H.; Rehman, A.; Lee, J.-K.; Seok, S. I.; Park, S.-J. Stabilization of perovskite solar cells: Recent developments and future perspectives. *Adv. Mater.* **2022**, *34*, No. 2204380.

(8) Qi, M.; Jin, L.; Yao, H.; Xu, Z.; Cheng, T.; Chen, Q.; Zhu, C.; Bai, Y. Recent progress on electrical failure and stability of perovskite solar cells under reverse bias. *Acta Physico-Chimica Sinica* **2025**, *41*, No. 100088.

(9) Chen, C.-H.; He, X.-Y.; Qin, R.-H.; Wang, K.-L.; Huang, L.; Jin, R.-J.; Chen, X.; Bian, Z.-K.; Yang, Y.-T.; Jin, K.; Chen, J.; Xia, Y.; Yavuz, I.; Wang, Z.-K. Reliable perovskite indoor photovoltaics for self-powered devices. *National Science Review* **2025**, *12*, 242.

(10) Duan, Y.; Chen, Y.; Wu, Y.; Liu, Z.; Liu, S.; Peng, Q. A comprehensive review of organic hole-transporting materials for highly efficient and stable inverted perovskite solar cells. *Adv. Funct. Mater.* **2024**, *34*, No. 2315604.

(11) Shin, Y. S.; Lee, J.; Sung, M. J.; Jeon, I.; Jeon, N. J.; Kim, D. S. Intrinsic and extrinsic determinants of stability in spiro-ometad-based hole-transporting layers in perovskite solar cells: Mechanistic insights and strategic perspectives. *Adv. Mater.* **2025**, *37*, No. e13270.

(12) Liu, S.; Miao, T.; Zhang, Y.; Liu, Z.; Chen, W.; Park, N.-G. Progress in high-efficiency inverted perovskite solar cells: Charge transport, interface engineering, and stability. *ACS Energy Letters* **2026**, *11*, 3121−3147.

(13) Vanin, F.; Webb, T.; Gao, D.; Welch, K.; Tremlett, W. D. J.; Qian, L.; Zhang, C.; Brown, R. K.; White, A. J. P.; Gasparini, N.; Bo, L.; Zhu, Z.; Haque, S. A.; Long, N. J. Stable comprehensive dopants for efficient and scalable perovskite solar cells. *Joule* **2026**, *10*, No. 102310.

(14) Zhang, T.; Wang, F.; Kim, H.-B.; Choi, I.-W.; Wang, C.; Cho, E.; Konefal, R.; Puttisong, Y.; Terado, K.; Kobera, L.; Chen, M.; Yang, M.; Bai, S.; Yang, B.; Suo, J.; Yang, S.-C.; Liu, X.; Fu, F.; Yoshida, H.; Chen, W. M.; Brus, J.; Coropceanu, V.; Hagfeldt, A.; Brédas, J.-L.; Fahlman, M.; Kim, D. S.; Hu, Z.; Gao, F. Ion-modulated radical doping of spiro-ometad for more efficient and stable perovskite solar cells. *Science* **2022**, *377*, 495−501.

(15) Huang, H.; Lan, Z.; Yang, Y.; Yan, H.; Wan, M.; Lu, Y.; Qu, S.; Jiang, T.; Sun, C.; Liu, B.; Cui, P.; Li, M. Controllable electrolysis doping of organic semiconductors for stable perovskite solar cells. *Joule* **2025**, *9*, No. 102106.

(16) Lan, Z.; Huang, H.; Du, S.; Lu, Y.; Sun, C.; Yang, Y.; Zhang, Q.; Suo, Y.; Qu, S.; Wang, M.; Wang, X.; Yan, L.; Cui, P.; Zhao, Z.; Li, M. Cascade reaction in organic hole transport layer enables efficient perovskite solar cells. *Angew. Chem., Int. Ed.* **2024**, *63*, No. e202402840.

(17) Urieta-Mora, J.; Choi, S. J.; Jeong, J.; Orecchio, S.; García-Benito, I.; Pérez-Escribano, M.; Calbo, J.; Zheng, L.; Byun, M.; Song, S.; Kim, G.-H.; Zakeeruddin, S. M.; Yoon, S.-Y.; Jo, Y.; Molina-Ontoria, A.; Ortí, E.; Martín, N.; Grätzel, M. Spiro-phenothiazine hole-transporting materials: Unlocking stability and scalability in perovskite solar cells. *Adv. Mater.* **2025**, No. e05475.

(18) Chen, J.; Yao, J.-W.; Wang, K.-L.; Bian, Z.-K.; Qiao, M.-Z.; Chen, C.-H.; Huang, L.; Xia, Y.; Fan, J.; Wang, Z.-K. Homogeneous interfacial ion-chelation for stable perovskite photovoltaics. *Matter* **2026**, *9*, No. 102581.

(19) Yu, S.; Xiong, Z.; Zhou, H.; Zhang, Q.; Wang, Z.; Ma, F.; Qu, Z.; Zhao, Y.; Chu, X.; Zhang, X.; You, J. Homogenized niox nanoparticles for improved hole transport in inverted perovskite solar cells. *Science* **2023**, *382*, 1399−1404.

(20) Chen, H.; Cao, Q.; Pu, X.; Zhao, Q.; He, X.; Zhou, Z.; Wang, T.; Feng, G.; Yin, R.; Chen, Z.; Tajibaev, I.; Boynazarov, I.; Bai, Y.; Jia, S.; Li, X. Strong coupling of niox and self-assembled molecules via inserted reductant for high-performance inverted perovskite solar cells. *Adv. Mater.* **2025**, *37*, No. e10553.

(21) Qu, S.; Sun, C.; Yang, F.; Huang, H.; Du, S.; Jiang, T.; Zhang, Q.; Yan, L.; Lan, Z.; Yang, Y.; Wang, Z.; Cui, P.; Li, M. Contextualized synthesis of phenanthroline-based isomeric linkers at heterointerfaces enables stable inverted perovskite solar cells. *Matter* **2026**, *9*, No. 102525.

(22) Liu, S.; Li, J.; Xiao, W.; Chen, R.; Sun, Z.; Zhang, Y.; Lei, X.; Hu, S.; Kober-Czerny, M.; Wang, J.; Ren, F.; Zhou, Q.; Raza, H.; Gao, Y.; Ji, Y.; Li, S.; Li, H.; Qiu, L.; Huang, W.; Zhao, Y.; Xu, B.; Liu, Z.; Snaith, H. J.; Park, N.-G.; Chen, W. Buried interface molecular hybrid for inverted perovskite solar cells. *Nature* **2024**, *632*, 536−542.

(23) Tian, C.; Sun, A.; Chen, J.; Zhuang, R.; Chen, C.; Zheng, J.; Liu, S.; Du, J.; Chen, Q.; Cai, L.; Han, S.; Tian, F.; Chen, C.-C. Photostable donor−acceptor interface for minimizing energy loss in inverted perovskite solar cells. *Nat. Photonics* **2026**, *20*, 287−295.
(24) Fei, C.; Zhang, Y.; Wang, M.; Yang, Y.; Shi, X.; Wang, S.; Guo, H.; Guo, C.; Liu, H.; Li, M.; Gu, H.; Barlow, S.; You, W.; Wang, M.; Marder, S. R.; Huang, J. Limiting phosphonic acid interlayer−perovskite reactivity to stabilize perovskite solar modules. *Science* **2026**, *391*, No. eadz7969.
(25) Cui, Z.; Li, W.; Feng, B.; Li, Y.; Sun, N.; Zhang, W.; Fu, S.; Li, X.; Fang, J. Thickness-insensitive polymeric hole-transporting layer for efficient inverted perovskite solar cells. *Joule* **2025**, *9*, No. 102011.
(26) Cen, T.; Zhuang, R.; Tian, C.; Sun, A.; Chen, Q.; Huang, R.; Zhao, Y.; Zhao, K.; Xue, T.; Li, R.; Chen, S.; Ni, H.; Zhao, T.; Chen, C.-C. Strengthening substrate anchoring of polymeric self-assembled monolayers for efficient and stable inverted perovskite solar cells. *Adv. Mater.* **2026**, *38*, No. e72622.
(27) Mai, S.; Suo, Z.-Y.; Lu, C.; Xiao, G.-B.; Mu, X.; Yang, F.; Tang, Y.; Cao, J. A synthetically tailored conjugated polymer for thermal and charge management in perovskite interfaces. *Nature Synthesis* **2026**, 1.
(28) Ma, M.; Bi, W.; Chu, Y.; Lv, J.; Po-Chuan, Y.; Zhang, Z.; Hong, L.; Mao, P.; Zhong, Y. Rapping up perovskite solar cells with polymers: A flexible point of view. *Adv. Funct. Mater.* **2025**, *35*, No. 2419067.
(29) Hu, X.; Wang, L.; Luo, S.; Yan, H.; Chen, S. Polymeric charge-transporting materials for inverted perovskite solar cells. *Adv. Mater.* **2025**, *37*, No. 2412327.
(30) Ahmed, Y.; Wang, W.; Kokaba, M. R.; Amaro, A.; Yeddu, V.; Gartside, H.; Awais, M.; Dayneko, S.; Zhang, D.; Parkin, H. C.; et al. Ptaa/perovskite contact-area reduced solar modules. *ACS Energy Letters* **2025**, *10*, 3306−3314.
(31) Bi, H.; Fujiwara, Y.; Kapil, G.; Tavgeniene, D.; Zhang, Z.; Wang, L.; Ding, C.; Sahamir, S. R.; Baranwal, A. K.; Sanehira, Y.; Takeshi, K.; Shi, G.; Bessho, T.; Segawa, H.; Grigalevicius, S.; Shen, Q.; Hayase, S. Perovskite solar cells consisting of ptaa modified with monomolecular layer and application to all-perovskite tandem solar cells with efficiency over 25%. *Adv. Funct. Mater.* **2023**, *33*, No. 2300089.
(32) Ding, Y.; Zhang, L.; Xie, P.; Zhang, Z.; Qu, G.; Xu, Z.-X. Synergistic bulk and interface passivation via conjugated ionic additives enables 26% efficient ptaa-based perovskite solar cells. *Adv. Energy Mater.* **2025**, No. e04647.
(33) Wang, T.; Qiao, L.; Ye, T.; Kong, W.; Zeng, F.; Zhang, Y.; Sun, R.; Zhang, L.; Chen, H.; Zheng, R.; Yang, X. Efficient and scalable perovskite solar cells achieved by buried interface engineering. *Journal of Materials Chemistry A* **2022**, *10*, 18014−18020.
(34) Heo, J. H.; Hong, S. Y.; Park, J. K.; Lee, H. J.; Zhang, F.; Im, S. H. Chemical oxidization of ptaa enables stable slot-die-coated perovskite solar modules. *Joule* **2025**, *9*, No. 101850.
(35) Xu, Y.; Xiong, S.; Jiang, S.; Yang, J.; Li, D.; Wu, H.; You, X.; Zhang, Y.; Ma, Z.; Xu, J.; Tang, J.; Yao, Y.; Sun, Z.; Bao, Q. Synchronous modulation of defects and buried interfaces for highly efficient inverted perovskite solar cells. *Adv. Energy Mater.* **2023**, *13*, No. 2203505.
(36) Luo, X.; Gao, D.; Zhang, D.; Zhou, G.; Guo, Y.; Zhang, C.; Zhu, Z.; Xu, B. Highly soluble and oxidizing organic salts doped hole-transporting layer enables efficient and stable perovskite solar cells. *Adv. Funct. Mater.* **2025**, *35*, No. 2425038.
(37) Nishimura, N.; Hinuma, Y.; Kanda, H.; Yamamoto, K.; Takada, H.; Yumoto, M.; Serien, D.; Tashiro, K.; Narazaki, A.; Murakami, T. N. Spontaneous perovskite passivator featuring dual functional groups. *Adv. Energy Mater.* **2026**, *16*, No. e06494.
(38) Wan, Z.; Yu, W.; Yang, J.; Zhang, Y.; Wang, Y.; Wei, R.; Azam, M.; Luo, J.; Jia, C. A non-ionic fluorinated p-dopant enables the construction of efficient and stable perovskite solar cells. *Chemical Science* **2025**, *16*, 16339−16346.
(39) Liu, Y.; Liu, Z.; Lee, E.-C. High-performance inverted perovskite solar cells using doped poly(triarylamine) as the hole transport layer. *ACS Applied Energy Materials* **2019**, *2*, 1932−1942.

https://doi.org/10.1021/acs.jpclett.6c02136
J. Phys. Chem. Lett. XXXX, XXX, XXX−XXX